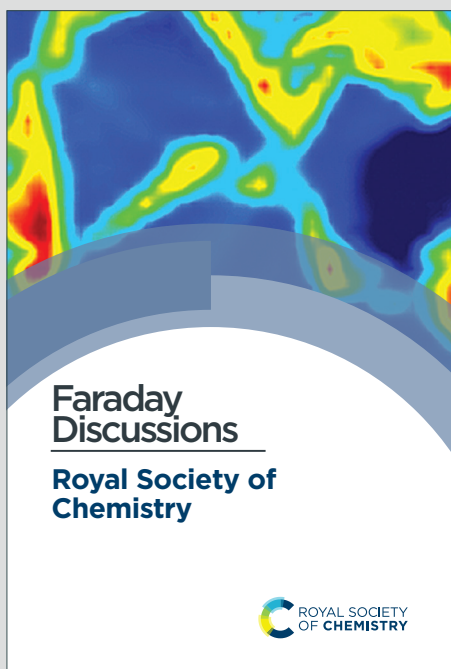


# Faraday Discussions

Accepted Manuscript



This is an Accepted Manuscript, which has been through the Royal Society of Chemistry peer review process and has been accepted for publication.

Accepted Manuscripts are published online shortly after acceptance, before technical editing, formatting and proof reading. Using this free service, authors can make their results available to the community, in citable form, before we publish the edited article. We will replace this Accepted Manuscript with the edited and formatted Advance Article as soon as it is available.

You can find more information about Accepted Manuscripts in the [Information for Authors](#).

Please note that technical editing may introduce minor changes to the text and/or graphics, which may alter content. The journal's standard [Terms & Conditions](#) and the [Ethical guidelines](#) still apply. In no event shall the Royal Society of Chemistry be held responsible for any errors or omissions in this Accepted Manuscript or any consequences arising from the use of any information it contains.

This article can be cited before page numbers have been issued, to do this please use: A. Hockmann, F. Ackermann, D. Diddens, I. Cekic-Laskovic and M. Schönhoff, *Faraday Discuss.*, 2024, DOI: 10.1039/D4FD00012A.

## ARTICLE

## Heterogeneous Li coordination in Solvent-in-Salt electrolytes enables high Li transference numbers

Anne Hockmann<sup>a, b</sup>, Florian Ackermann<sup>a, c</sup>, Diddo Diddens<sup>a, d</sup>, Isidora Cekic-Laskovic<sup>d</sup>, Monika Schönhoff<sup>\*a</sup>

Received 00th January 20xx,  
Accepted 00th January 20xx

DOI: 10.1039/x0xx00000x

The transport properties and the underlying coordination structure of a ternary electrolyte consisting of lithium bis(trifluoromethanesulfonyl)imide (LiTFSI), 1,2-dimethoxyethane (DME), and 1,3-dioxolane (DOL) is studied over a wide concentration range up to a Solvent-in-Salt (SiS) electrolyte. Among other advantages for next-generation battery application, SiS electrolytes offer high lithium transference numbers ( $t_{\text{Li}}$ ) of 0.73. We analyze the transport mechanism by electrophoretic NMR (eNMR), providing mobilities  $\mu_i$  of all species. Intriguingly, in the SiS region, the mobility of the neutral species DME exceeds the cation mobility ( $\mu_{\text{DME}} > \mu_{\text{Li}}$ ), suggesting a heterogeneous transport mechanism, where the  $\text{Li}^+$  mobility is averaged over different species. Based on Raman spectroscopy, NMR spectroscopy and MD simulations, we derive a model for a concentration-dependent  $\text{Li}^+$  coordination environment with a heterogeneous  $\text{Li}^+$  coordination in the SiS region, where the 1<sup>st</sup> coordination shell either consists of TFSI<sup>-</sup> and DOL only, or of DME, TFSI<sup>-</sup>, and DOL. Lithium ions partially coordinated by DME migrate faster in an electric field, in contrast to lithium ions solely coordinated by anions and DOL molecules, explaining the peculiarity of the rapidly migrating neutral DME molecules. Further, DME is identified as an exclusive bidentate ligand, while TFSI<sup>-</sup> and DOL act as bridging ligands coordinating different  $\text{Li}^+$  ions. Thus,  $\text{Li}^+$  coordination heterogeneity is the basis for  $\text{Li}^+$  transport heterogeneity and for achieving very high  $\text{Li}^+$  transference numbers. In addition, an effective dynamic decoupling of  $\text{Li}^+$  and anions occurs with an Onsager coefficient  $\sigma_{\infty} \approx 0$ . These results provide a deeper understanding of the very efficient lithium ion transport in SiS electrolytes with potential to bring further improvements for battery applications.

### Introduction

The pursuit for next generation batteries beyond the established Li-ion technology is driven by the need for high energy densities in mobile applications, but also for safer and more environmentally friendly battery cell chemistries. The aim is to increase the overall performance of batteries while enabling a more sustainable product life cycle e.g. by using abundant transition metals in the electrode materials, and focusing on energy efficient cell production.<sup>1</sup> The introduction of alternative active materials, however, imposes a range of new requirements towards the whole battery cell chemistry. The liquid electrolyte, as the only component physically interfacing every other battery cell component, governs the

overall performance and safety of the resulting chemistry by simultaneously coping with issues arising from the active materials, e.g. dendrite growth, exfoliation, or active material loss. In the case of lithium sulfur (LiS) batteries, highly concentrated liquid electrolytes are considered as promising candidates to overcome these drawbacks. Due to the high conducting salt concentration, they comprise no non-coordinating solvents and exhibit an anion-rich lithium solvation shell leading to several advantages like a broader thermal and electrochemical stability, a robust inorganic SEI, the suppression of lithium dendrite growth and dissolution of polysulfides. Moreover, this unique solvation structure results in a high rate capacity, improved galvanostatic cycling, a high Coulombic efficiency, and a high level of safety. In addition, high lithium transference numbers  $t_{\text{Li}}$  of up to 0.7 were reported for different high concentration electrolytes, which is notably higher than values ranging from 0.2 to 0.4 observed in common dilute and moderate concentrated electrolytes.<sup>2-7</sup>

On the other hand, high concentration electrolytes suffer from a high viscosity and low ionic conductivity.<sup>8-14</sup> Though conductivity is a vital bulk property of each battery electrolyte, however, it is not decisive for the overall electrochemical performance as indicated by the relevant key performance indicators. The latter include parameters such as high specific capacity, capacity retention, Coulombic efficiency and suppressed lithium dendrite formation, which can be achieved

<sup>a</sup> Institute of Physical Chemistry, University of Münster, Corrensstraße 28/30, 48149 Münster, Germany. E-mail: schoenho@uni-muenster.de

<sup>b</sup> International Graduate School Battery Chemistry, Characterization, Analysis, Recycling, and Application (BACCARA), University of Münster, Corrensstraße 40, 48149 Münster, Germany.

<sup>c</sup> Current address: BASF SE, Carl-Bosch-Straße 38, 67056 Ludwigshafen/Rhein, Germany.

<sup>d</sup> Helmholtz Institute Münster, IEK-12, Forschungszentrum Jülich GmbH, Corrensstraße 48, 48149 Münster, Germany.

† Electronic Supplementary Information (ESI) available: Pdf file containing densities, ionic conductivities, relaxation rates for all species, eNMR phase shifts, deconvolution of Raman spectra, diffusion data, NMR spectra, histograms of the molecular coordination number, and snapshots of the MD simulation box. See DOI: 10.1039/x0xx00000x



in high concentration electrolytes, and make them interesting candidates for application.<sup>15, 16</sup>

The reported particularly high lithium transference numbers in high concentration electrolytes are generally attributed to a change in the lithium transport mechanism due to ionic aggregates. However, distinct differences regarding the dominant transport mechanism are reported in dependence on the used conducting salts and solvents. On the one hand Borodin et al. showed a nano-heterogeneity in an aqueous electrolyte, with relatively immobile anion-rich domains and aqueous Li<sup>+</sup>-conducting percolating channels.<sup>17</sup> On the other hand, Dokko et al. and Nakanishi et al. reported an enhanced  $t_{\text{Li}}$  for sulfolane-based electrolytes, postulating an ion hopping mechanism supported by a chainlike lithium ion coordination of the anions and sulfolane molecules.<sup>4, 18</sup> A similar mechanism was proposed by Kondou et al. for two keto ester-based systems, which are also able to act as bridging ligands similar to sulfolane. However, when methyl levulinate (ML) was used as the solvent this transport mechanism was not observed but rather a less effective vehicular transport, since ML coordinates lithium bidentate in contrast to sulfolane.<sup>19</sup> Finally, Self et al. studied a propylene carbonate-based electrolyte containing two different lithium salts. They found that ion hopping and ligand exchange take place in the system, too. However, vehicular transport still exists and is strongly dependent on the conducting salt used. Therefore, the vehicular transport mostly accounts for the efficiency of the ion transport.<sup>7</sup> Overall, these examples show that the ion transport mechanism strongly depends on the coordination properties of the used conducting salt and solvent molecules.

In 2013, Suo et al. published an article in which, in contrast to the systems discussed above, an electrolyte comprising two different ethereal solvents, namely 1,2-dimethoxyethane (DME) and 1,3-dioxolane (DOL), is used.<sup>17</sup> As the conducting salt, they used lithium bis(trifluoromethanesulfonyl)imide (LiTFSI). Additionally, they defined Solvent-in-Salt (SiS) electrolytes as a class of concentrated salt solutions, in which the salt-to-solvent ratio by volume and/or mass exceeds unity.<sup>20, 21</sup> In this region, they also reported surprisingly high  $t_{\text{Li}}$  up to 0.73. Raman studies showed strong lithium-anion clustering, which led to the suggestion that the observed high lithium transference number is caused by "Li-ion exchange between aggregated ion pairs and solvent molecules", assuming a Li transport similar to the mechanism in PEO.<sup>22</sup> However, the role of the two different solvent molecules, and consequently the exact transport mechanism is not yet fully understood. Since the above discussed articles clearly show that the lithium transport mechanism in highly concentrated liquid electrolytes strongly depends on the coordination properties of the used components, it is crucial to investigate the bi-solvent electrolyte formulation reported by Suo et al.<sup>19</sup> in more detail. In this work, a concentration series of LiTFSI dissolved in a 1:1 (vol:vol) mixture of DME and DOL at molal concentrations ranging from 1-7 M, according to Suo et al.,<sup>5</sup> is investigated. It is the aim to gain a deeper understanding of the mechanisms causing the reported highly efficient lithium transport. Therefore, electrophoretic NMR (eNMR) is applied, which is a

versatile technique for the direct determination of a molecule's drift velocity in an electric field.<sup>19, 23</sup> The species-selective transport behavior of all molecular components is analyzed based on the Li<sup>+</sup> coordination environment, as characterized by various spectroscopic methods. Additionally, molecular dynamics (MD) simulations are performed and compared to the experimental results. From the obtained results, a model description of the average first coordination shell of lithium in dependence on the conducting salt concentration is derived. In particular, the mobilities obtained from eNMR exhibit a positive mobility of the neutral species DME in the SiS domain, which exceeds the mobility of Li<sup>+</sup>. Combined with the observed exclusive bidentate coordination of DME in contrast to the bridging ligands DOL and TFSI, this suggests a heterogeneous lithium coordination with consequences for transport: Lithium cations containing DME in their coordination exhibit larger drift velocities as compared to cations coordinated only by anions and DOL, since the latter are more strongly coordinated to neighboring cations at high salt concentrations. Therefore, these results serve as an explanation for the reported high  $t_{\text{Li}}$  values.

## Experimental

### Materials and sample preparation

The conducting salt lithium bis(trifluoromethanesulfonyl)imide (LiTFSI, Sigma-Aldrich, 99%, dried at 100 °C and high vacuum overnight) was dissolved in a 1:1 mixture by volume of the solvents 1,3-dioxolane (DOL, Sigma-Aldrich, 99.8%, anhydric, ~ 75 ppm BHT as inhibitor, used as received) and 1,2-dimethoxyethane (DME, Sigma-Aldrich, > 99.5%, anhydric, used as received). Samples with molal conducting salt concentrations (see eq. S1) between 1 and 7 mol L<sup>-1</sup> were prepared and handled in a glove box under argon atmosphere. The corresponding molar LiTFSI concentrations and oxygen-to-lithium ratios were determined via density measurements (Rudolph Research Analytical DDM 2910) at 26.5 °C and are given in Table S1 in the supporting information.

### NMR experiments

All NMR experiments for the nuclei <sup>1</sup>H, <sup>7</sup>Li, and <sup>19</sup>F, except electrophoretic mobility measurements and some diffusion measurements taken at 30 °C, were conducted at 26.5 °C on a Magritek Spinsolve spectrometer operating at 60 MHz <sup>1</sup>H frequency and providing magnetic field gradients up to 0.16 T/m.

### Spin relaxation

The longitudinal spin relaxation time  $T_1$  was obtained performing inversion recovery experiments.<sup>23</sup> Employing the Carr-Purcell-Meiboom-Gill (CPMG) experiment the transversal relaxation time  $T_2$  was determined, using a delay  $\tau$  between 180° pulses of 1 ms.<sup>19, 24</sup> The maximal delay was adjusted to the respective nucleus and sample (<sup>1</sup>H: 1 to 3 s; <sup>19</sup>F: 2 to 5 s; <sup>7</sup>Li: 2 to 25 s).



### PFG-NMR diffusion

The self-diffusion coefficients  $D$  were determined via Pulsed Field Gradient (PFG) NMR using the pulsed gradient stimulated echo sequence.<sup>25</sup> For each sample and investigated nucleus the pulse duration and maximal gradient strength were adjusted and the observation time  $\Delta$  was set to 100 ms. Additionally, the measurements were reproduced using a shorter  $\Delta$  of 50 ms to exclude convection artefacts. Diffusion experiments were conducted at 26.5 °C at 60 MHz and at 30 °C at 400 MHz in combination with the electrophoretic experiments, see below.

### Electrophoretic NMR (eNMR)

Electrophoretic mobilities  $\mu$  were determined employing eNMR, using a 400 MHz Bruker Avance III HD spectrometer and a sample holder with electrodes as described earlier.<sup>26</sup> A double stimulated echo pulse sequence was employed for convection compensation,<sup>27</sup> where the electric field is inverted in between the second and third magnetic field gradient pulse.<sup>28</sup> A recycle delay of 60 s between scans allows for dissipation of heat generated by Joule heating. The observation time was 100 ms, the gradient pulse durations were 1 ms (<sup>1</sup>H and <sup>19</sup>F), and 3 ms (<sup>7</sup>Li), and the temperature is  $T = 30$  °C. The gradient strength was kept constant during the experiment at a value chosen appropriately for each sample and nucleus, in order to achieve a high phase shift while maintaining a reasonable signal-to-noise ratio. In each experiment, the applied voltage was incremented from low to high values with an alternating sign of the first pulse. The resulting eNMR spectra were evaluated via an approximation by phase sensitive Lorentzian profiles, as described earlier.<sup>29</sup> In the fit procedure the phases of <sup>1</sup>H resonances corresponding to the same molecule were set to equal values. The voltage dependent phase shift  $\phi - \phi_0$  was determined as the difference of the determined phase angle at a given voltage to the phase angle at 0 V. The phase shift is linearly dependent on the gyromagnetic ratio  $\gamma$ , the magnetic field gradient strength  $G$  and duration  $\delta$ , the observation time between the encoding and decoding gradient pulses  $\Delta$ , the electrophoretic mobility  $\mu$ , and the applied electric field  $E$ , which is given by the applied voltage divided by the electrode distance  $d$ . In contrast to battery cell experiments, polarization effects can be neglected due to the short electric field pulses, and the full potential applies to the sample, see also consistency with impedance data in supporting information, Figure S1.

$$\phi - \phi_0 = \gamma \delta \Delta G \mu \frac{U}{d} \quad (1)$$

The electrophoretic mobility was determined from a linear approximation according to eq. 1. Three independent measurements on different samples are performed for each sample and nucleus and the resulting mobilities averaged.

### Impedance spectroscopy

All impedance spectroscopy (IS) measurements were conducted at 30 °C using a frequency analyzer (*Novocontrol Alpha*, Montabaur, Germany), and an in-house built symmetrical sample cell made of white copper with gold-coated

electrodes. Each experiment was conducted with a voltage amplitude of 10 mV. The conductivity of each respective electrolyte was determined from the dc plateau under the assumption of a sample cell behavior described by the *Randles* circuit in absence of faradaic reactions.<sup>25</sup>

### Raman spectroscopy

Raman spectra were taken on a MultiRAM FT-Raman spectrometer (Bruker, Ettlingen). The laser had a wavelength of 1064 nm and a power of 263 mW. The samples were measured in a NMR tube with a resolution of 1 cm<sup>-1</sup> in a range of 30-3600 cm<sup>-1</sup>. Raman bands for vibrations of TFSI<sup>-</sup> (~445 cm<sup>-1</sup>), DME (~840 cm<sup>-1</sup>), and DOL (~940 cm<sup>-1</sup>) were baseline corrected and deconvoluted using the software OPUS 8.5 (Bruker). Deconvolution yields two, three, or three peaks, respectively, each a combination of 40% Gauss and 60% Lorenz line shapes. The peaks were assigned to resonances for uncoordinated and coordinated TFSI<sup>-</sup>, DME and DOL, respectively. Their respective integrals,  $A_{\text{coord}}$  and  $A_{\text{free}}$ , were employed to calculate the coordinated fraction,  $f_{\text{coord}}$ , according to a procedure described earlier, which assumes equal Raman scattering coefficients of the free and coordinated species.<sup>30-32</sup>

$$f_{\text{coord,Raman}} = \frac{A_{\text{coord}}}{A_{\text{free}} + A_{\text{coord}}} \quad (2)$$

### MD simulations

The MD simulations were run using the software package GROMACS (version 2019.3)<sup>33</sup> with OPLS-AA force field<sup>34</sup> for the solvents and CL&P force field<sup>34, 35</sup> for the ions. The evaluation was performed using routines written in Python 3.7.2 based on the MDAnalysis package.<sup>36, 37</sup> Initially, a cubic simulation box with about 1000 molecules was generated by means of PACKMOL (version 20.010).<sup>38</sup> After this initialization, a relaxation run was produced at 426.85 °C for 10 ns. The equilibration was performed at the target temperature 26.5 °C generating 100 ns. The simulation time of the final production run was 1  $\mu$ s. The simulations were run for four compositions with molal concentrations of 1 M, 3 M, 5 M, and 7 M. To implicitly include polarization effects, the partial charges of the ions were scaled by a factor of 0.8 as reported elsewhere for similar systems.<sup>39-44</sup>

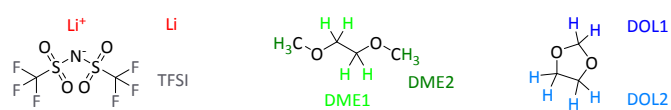
## Results and discussion

Li salt/DOL/DME electrolyte formulations are investigated in a wide range of concentrations, spanning the transition from Salt-in-Solvent to Solvent-in-Salt. First of all, transport measurements highlight the specific features of ion transport in Solvent-in-Salt electrolytes. To access the transport of all constituent species, we performed species-selective NMR transport measurements. To distinguish between the different NMR active nuclei of the electrolyte systems, they are labelled as illustrated in Scheme 1.

### Diffusion and spin relaxation



In the range from 1 to 7 mol L<sup>-1</sup>, the self-diffusion coefficients  $D$  for cations, anions, and solvent molecules are obtained by PFG-



**Scheme 1** Molecular structures and labelling of investigated nuclei in <sup>1</sup>H, <sup>7</sup>Li and <sup>19</sup>F NMR.

NMR (Fig. 1a). For all species,  $D$  decreases with increasing conducting salt concentration. This can be mainly interpreted as an overall decrease of system dynamics, which is very common for electrolytes.<sup>43, 44</sup> Moreover, over the whole concentration range, one observes equal diffusion coefficients of Li<sup>+</sup> and TFSI<sup>-</sup>. Whether this equality is a coincidence, or whether it suggests correlated diffusion of Li<sup>+</sup> and TFSI<sup>-</sup> in form of ion pairs, can be judged by calculating the ionicity. The ionicity, or inverse Haven ratio  $H_R^{-1}$ , is obtained from eq. 3, where  $\sigma$  corresponds to the ionic conductivity measured by IS, and  $\sigma_{NE}$  is the ionic conductivity estimated from the self-diffusion coefficients using the Nernst-Einstein equation (eq. 4) with the charge number  $z_i$ , the concentration  $c_i$ , and the self-diffusion coefficient  $D_i$  of the ionic species, as well as the temperature  $T$ , the Faraday constant  $F$  and the Gas constant  $R$ .

$$H_R^{-1} = \frac{\sigma}{\sigma_{NE}} \quad (3)$$

$$\sigma_{NE} = \left(\frac{F^2}{RT}\right) \sum_i z_i^2 c_i D_i \quad (4)$$

The conductivity data from IS are shown in the SI, Fig. S1a, and largely agree to earlier data by Suo et al.<sup>43</sup> The values for  $\sigma_{NE}$  are substantially larger (see comparison in Fig. S1a), and consequently the ionicities are low, in the range of 0.2 to 0.3

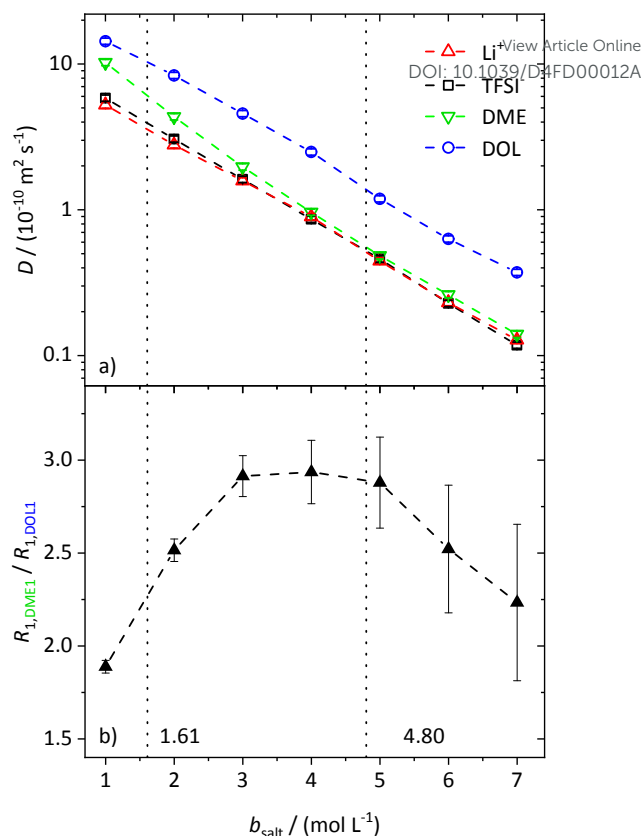


**Fig. 1** a) Self-diffusion coefficients  $D$  of the investigated species obtained by PFG-NMR in dependency on the molal salt concentration. b) Ratios of the  $R_1$  relaxation rates of the solvent protons. The dashed lines in both graphs serve as guide to the eye, and the vertical dotted lines result from a model-based interpretation, marking different regimes of the lithium coordination shell.

(see SI, Fig. S1b). These low values highlight the non-ideality of the electrolyte exhibiting a low dissociation degree and strong ion correlations.

While the self-diffusion coefficient of both ions is almost identical, distinct differences can be noticed in the diffusion of the solvent molecules. Fig. 1a shows that  $D_{DME}$  is more strongly affected by an increasing amount of salt than DOL and approaches the values of the ions for high conducting salt concentrations. This is not the case for DOL, where  $D_{DOL}$  exceeds  $D_{Li}$  by the same factor, irrespective of salt concentration. Therefore, DME seems to coordinate to Li<sup>+</sup> rather than DOL, leading to a smaller fraction of free DME molecules, and a higher similarity of the diffusion coefficients of DME and the ions.

The assumption of a preferred coordination of Li<sup>+</sup> cations by DME molecules is evaluated by analyzing the spin-lattice relaxation rates  $R_1$  of the protons of the two solvent molecules. First of all, the spin-lattice and spin-spin relaxation rates,  $R_1$  and  $R_2$ , of all species in the electrolyte system increase with an increasing salt concentration due to the generally slowed down dynamics. These trends are shown and explained in more detail in the SI (see Fig. S2). However, by investigating the ratio of the relaxation rates  $R_1$  of the protons of the two different solvent species (see Fig. 1b for the protons DME1 and DOL1 according



to Scheme 1), the influence of the general effect of slowed down dynamics is eliminated, such that variations of the local coordination environment of the solvent molecules can be identified.

With values from 1.6 to 3.0 the ratio does not vary strongly over the whole conducting salt concentration range, while the relaxation rates vary by an order of magnitude. This confirms that concentration-dependent variations of the overall system dynamics are largely compensated by forming the ratio. Nevertheless, a maximum around  $b_{\text{salt}} = 4 \text{ mol L}^{-1}$  is detected, which can be attributed to changes of the local dynamics of the individual solvent species with salt addition. We note that the system is in motional narrowing (see identity of  $R_1$  and  $R_2$  values of the same protons in Fig. S2b, where an increase of  $R_1$  indicates reduced local dynamics). Thus, at moderate conducting salt concentrations the DME local dynamics is more strongly reduced than that of DOL, while at conducting salt concentrations higher than 4.8 M, the dynamics of DOL is more affected. The considered electrolyte formulations with conducting salt concentrations exceeding 4.8 M fulfill the definition of a SiS electrolyte, therefore this concentration represents the starting point of the SiS region. Thus, again these trends indicate that at moderate salt concentrations DME coordinates  $\text{Li}^+$  rather than DOL, while DOL starts to participate in the coordination shell of the cation in the SiS region, leading to a stronger increase of its relaxation rate  $R_{1,\text{DOL}}$ . This coordination preference will be the basis of a later introduced stoichiometric model, see below.

### Electrophoretic mobilities

To characterize the migration of each of the molecular species in an electric field, eNMR is applied. In case of  $^1\text{H}$  eNMR a deconvolution of the partially overlapping DOL and DME resonances with their respective phase shifts is required, which is performed according to a previously established procedure.<sup>44</sup> Representative spectra are given in the SI, Fig. S3. The electrophoretic mobilities  $\mu$  obtained from  $^1\text{H}$ ,  $^7\text{Li}$  and  $^{19}\text{F}$  eNMR according to eq. 1 are shown in Fig. 2a. Conducting salt concentrations lower than 3 M are not measurable due to DOL polymerization in the electric field. The mobilities of the anion are negative over the whole conducting salt concentration range, which corresponds to a drift towards the positive electrode, while the opposite sign applies for the cation. This is in line with expectations, as well as the decrease of the absolute values of the mobility with increasing conducting salt concentration, similar to the self-diffusion coefficients in Fig. 1a. Regarding the solvents DME and DOL, a mobility of zero is measured for DOL at the lowest salt concentration of  $b_{\text{salt}} = 3 \text{ mol L}^{-1}$ , as expected for a neutral species. However, for

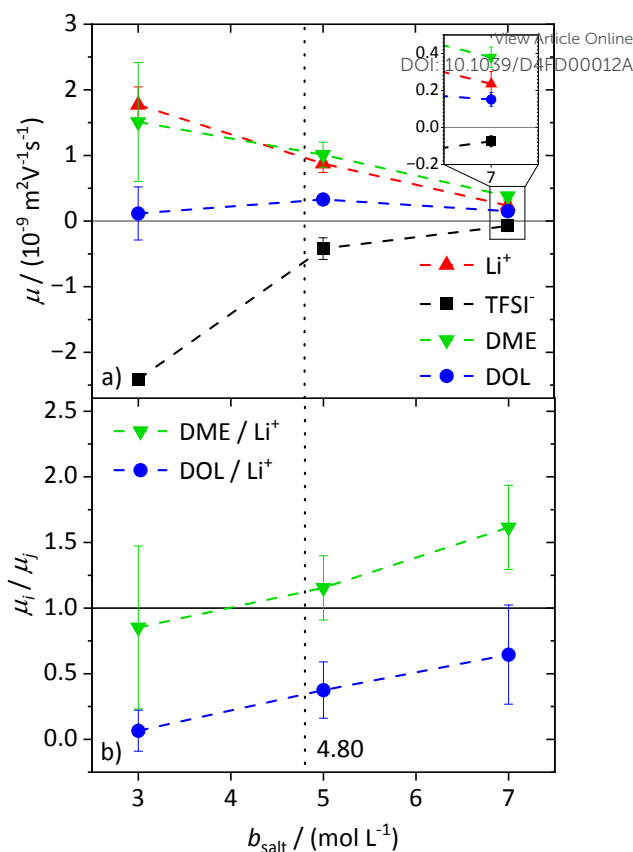


**Fig. 2** a) Electrophoretic mobilities  $\mu$  of  $\text{Li}^+$ ,  $\text{TFSI}^-$ , DME, and DOL, determined via  $^7\text{Li}$ ,  $^{19}\text{F}$ , and  $^1\text{H}$  eNMR, in dependency on the molal conducting salt concentration  $b_{\text{salt}}$ . b) DME/Li and DOL/Li electrophoretic mobility ratios  $\mu_i/\mu_j$  in dependency of the molal conducting salt concentration  $b_{\text{salt}}$ . The dashed lines in both graphs serve as guide to the eye, and the vertical dotted line results from a model-based interpretation, marking different regimes of the lithium coordination shell.

DME we observed a positive mobility, which is regarded as identical to  $\mu_{\text{Li}}$  within the observed error, leading to the assumption that DME not only coordinates the lithium cations, but even forms cationic clusters, so-called dynamic clusters, which form the cationic species migrating in the electric field. A migration of neutral species in an electric field was previously observed for solvate ionic liquids, where glyme- $\text{Li}^+$  complexes are sufficiently long-lived to constitute the migrating species.<sup>45</sup> A similar migration of DME with  $\text{Li}^+$  can be concluded here. For higher conducting salt concentrations,  $\mu_{\text{DOL}}$  also turns positive, implying that some of the DOL molecules coordinate and migrate with the cations. This is the case from  $b = 5 \text{ mol L}^{-1}$  on and confirms the onset of DOL coordination to  $\text{Li}^+$  in the SiS domain.

Interestingly for conducting salt concentrations in the SiS region, the mobility of DME is even higher than the mobility of lithium, see inset in Fig. 2a and Fig. 2b. This observation is unexpected, and implies that the neutral species DME migrates on average faster in the electric field than the lithium cation. The solvent-to-lithium mobility ratios increasing with conducting salt concentration, depicted in Fig. 2b, illustrate this clearly with the transition of  $\mu_{\text{DME}}/\mu_{\text{Li}}$  smaller than one to values



larger than one in the SiS concentration region. Furthermore, Fig. 2b shows that with increasing conducting salt concentration not only the DME but also the DOL mobility increases in relation to that of lithium. However, it does not exceed one and thus, it is likely that there is still a fraction of free and not migrating DOL molecules reducing the average mobility of this species compared to the cation.

### Transference numbers

The lithium transference numbers determined by eNMR and obtained from eq. 5,  $t_{\text{eNMR}}$ , and the transport number  $t_{\text{app}}$  obtained from diffusion NMR and calculated using eq. 6 are shown in Fig. 3.

$$t_{\text{eNMR}} = \frac{\mu_{\text{Li}}}{\mu_{\text{Li}} - \mu_{\text{TFSI}}} \quad (5)$$

$$t_{\text{app}} = \frac{D_{\text{Li}}}{D_{\text{Li}} + D_{\text{TFSI}}} \quad (6)$$

They are compared to  $t_{\text{abc}}$ , the transference number obtained by Suo et al. via potentiostatic measurements under anion blocking conditions. It is important to note that the three different transport coefficients describe different phenomena and properties of the electrolyte formulation. While  $t_{\text{eNMR}}$  describes the fraction of charge transport associated with species containing the  $^7\text{Li}$  nucleus in relation to the total conductivity of the solution, the transport number  $t_{\text{app}}$  is an approximation of the transference number, assuming fully dissociated electrolytes and neglecting ion correlations. For moderate conducting salt concentrations, between 1 and 4 M, the transference number  $t_{\text{eNMR}}$  equals the transport number  $t_{\text{app}}$  of 0.5. However, a steep increase is observed for both transference numbers for electrolytes in the SiS region. This mismatch signifies the relevance of dynamic correlations for highly concentrated electrolytes in the SiS domain.

On the other hand, the potentiostatic transference number  $t_{\text{abc}}$  describes the lithium current under anion blocking conditions in relation to the total current in the electrolyte, which is in good agreement with  $t_{\text{eNMR}}$ . We note that an agreement of  $t_{\text{abc}}$  and  $t_{\text{eNMR}}$  is not a general feature, as in concentrated electrolytes both quantities may differ largely, as they are affected by ion correlations in a different manner.<sup>19</sup>

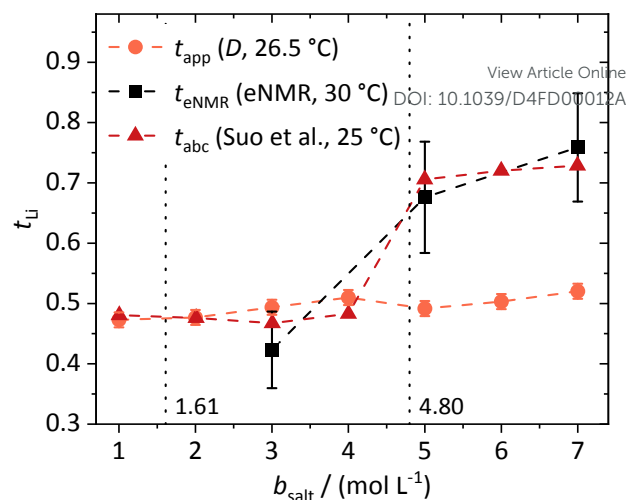


**Fig. 3** Lithium transference numbers in dependency of the molal conducting salt concentration  $b_{\text{salt}}$  determined via diffusion NMR, eNMR, and potentiostatic current measurements by Suo et al.<sup>46</sup> The dashed lines serve as guide to the eye, and the vertical dotted lines result from a model-based interpretation marking different regimes of the lithium coordination shell.

This difference is given by the dependency of  $t_{\text{abc}}$  and  $t_{\text{eNMR}}$  on the Onsager coefficients  $\sigma_{++}$ ,  $\sigma_{+-}$ , and  $\sigma_{--}$ , where the latter describe the dynamic correlations between the charged species:<sup>47</sup>

$$t_{\text{eNMR}} = \frac{\sigma_{++} - \sigma_{+-}}{\sigma_{++} + \sigma_{--} - 2\sigma_{+-}} = \frac{\sigma_{++} - \sigma_{+-}}{\sigma_{\text{ion}}} \quad (7)$$

$$t_{\text{abc}} = \frac{\sigma_{++} - \frac{(\sigma_{+-})^2}{\sigma_{--}}}{\sigma_{++} + \sigma_{--} - 2\sigma_{+-}} = \frac{\sigma_{++} - \frac{(\sigma_{+-})^2}{\sigma_{--}}}{\sigma_{\text{ion}}} \quad (8)$$

Therefore, an agreement of these transference numbers ( $t_{\text{abc}} = t_{\text{eNMR}}$ ), as observed here, implies:

$$\sigma_{--} = \sigma_{+-} \text{ or } \sigma_{+-} = 0. \quad (9)$$

We calculate the Onsager coefficients from the MD simulation results, which are discussed further below and used to elucidate the  $\text{Li}^+$  coordination environment. Since we realized deviations of the absolute values of dynamic quantities from experiment, especially at ultra-high conducting salt concentrations, we analyze the relative magnitude  $\sigma_{ij}$  normalized to  $\sigma_{\text{ion}}$ , see description in SI and Fig. S4.

We indeed find  $\sigma_{+-}/\sigma_{\text{ion}} \approx 0$  over the whole concentration range (see Fig. S4) explaining the peculiar agreement of  $t_{\text{abc}}$  and  $t_{\text{eNMR}}$ . The vanishing dynamic correlation of  $\text{Li}^+$  and anion implies an effective dynamic decoupling of the  $\text{Li}^+$  transport from anion transport. The combination with a strong increase of  $\sigma_{++}/\sigma_{\text{ion}}$  with concentration (see Fig. S4), evidencing a structural  $\text{Li}^+$  transport, yields a strong increase of the  $\text{Li}^+$  transference number.

From these dynamic findings, first conclusions on the concentration-dependent  $\text{Li}^+$  coordination environment can be drawn. With a reduction of the oxygen-to-lithium ratio, the ion coordination and consequently the ion transport changes to a mechanism favoring lithium. In dilute and moderate concentrated electrolytes,  $\text{Li}^+$  is migrating jointly with its first



coordination shell consisting of DME molecules, as discussed above, via a vehicular mechanism. This vehicle is of a similar size as the anion, which might lead to similar drift velocities and to a transference number of 0.5. With increasing conducting salt concentration, the DME concentration becomes insufficient to provide a full coordination of the lithium cations, thus the coordination environment of  $\text{Li}^+$  becomes heterogeneous, influencing the ion transport. The high lithium transference numbers of approximately 0.7 in the SiS region suggests that the mechanism of lithium transport is drastically changed, which we will analyze in detail by studying the coordination environment in the following sections. Interestingly, this change is accompanied by a transition of the DME/Li mobility ratio from  $< 1$  to  $> 1$ , see Fig. 2b.

### Raman spectra

In order to interpret the concentration-dependent lithium transport mechanisms based on a stoichiometric model for the  $\text{Li}^+$  coordination shell, we first analyze the local coordination environment of  $\text{Li}^+$  via Raman spectroscopy, chemical shifts in NMR spectra of the different molecules, and MD simulations. The vibrational Raman bands of the anion and of the two solvent molecules are shown in Fig. 4. The shown spectra are normalized to the molar fraction of salt. In case of the anion, depicted in Fig. 4a, the band at around  $742\text{ cm}^{-1}$  is assigned to free or only loosely coordinating anions, while the increasing band at  $747\text{ cm}^{-1}$  corresponds to coordinated or even

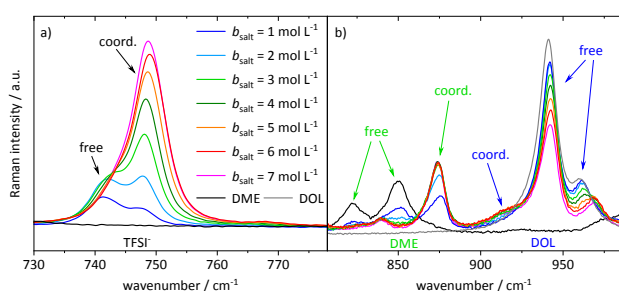


**Fig. 4** Stack plot of the Raman spectra of the electrolyte system at different conducting salt concentrations. a) vibration band of the anion and b) of the two solvent molecules.

aggregated anions.<sup>19, 32, 34, 48, 49</sup> Regarding Fig. 4b, the three bands around  $850\text{ cm}^{-1}$  arise from DME, with the two bands on the left assigned to free molecules, while the one on the right-hand side to an increasing amount of coordinated DME molecules.<sup>23, 50, 51</sup> Vibrational bands of DOL are observed around  $960\text{ cm}^{-1}$ , consistent with the grey line for pure DOL in Fig. 4b. The two intense bands correspond to free DOL molecules. In addition, we observe a small band at around  $910\text{ cm}^{-1}$ , which is increasing with salt concentration. To the best of our knowledge, this band was not reported earlier and we interpret it here as the vibration of coordinated DOL molecules. This is reasonable, as on the one hand a similar band arises for a concentrated electrolyte based on tetrahydrofuran<sup>52</sup> and on the other hand this band is increasing with the conducting salt concentration, while the other bands assigned to DOL decrease. Exemplary fits of the vibrational bands of the three coordinating

molecular species are presented in the SI (see Fig. S5). In the following section, the fractions of coordinating molecules  $f_{\text{coord.,Raman}}$  are calculated according to eq. 2 from the deconvoluted spectra.

### Average first coordination shell of lithium

In the following, we discuss the first coordination shell of the  $\text{Li}^+$  ions in dependence of conducting salt concentration based on the Raman bands, chemical shifts and coordination numbers obtained from MD simulation results. As all methods suggest a coordination preference in the order  $\text{DME} > \text{TFSI}^- > \text{DOL}$ , we assume a model for the average lithium coordination shell in dependence on the conducting salt concentration shown in Fig. 5a, where for dilute and moderate concentrated electrolytes  $\text{Li}^+$  is only coordinated by DME molecules. Here, three DME molecules, i.e. 6 oxygens, coordinate one lithium cation resulting in a lithium coordination number  $N_c = 6$ . A total coordination number of almost six over the whole concentration range is indicated by MD simulations, see Fig. 5b. This is in accordance to literature of different electrolytes, generally reporting a coordination number of 4-6 oxygens around lithium cations.<sup>51-55</sup> In the high concentrated region, above a  $1.61\text{ M}$  salt concentration, the concentration of DME is too low to provide  $N_c$  of six. Thus, the anions participate in the lithium coordination. When reaching the ultra-high concentrated SiS region, the stoichiometry of the electrolyte requires a further change of the average lithium coordination shell, since above  $b_{\text{salt}} = 4.80\text{ mol L}^{-1}$  the number of DME and  $\text{TFSI}^-$  oxygens becomes insufficient to fully coordinate  $\text{Li}^+$ . Here, also DOL has to coordinate to some extent to still achieve  $N_c = 6$ . Interestingly, this stoichiometric definition of the SiS region agrees well to the volumetric definition ( $V_{\text{salt}}/V_{\text{solvent}} > 1$ ), and to the onset of the high transference number regime, see Fig. 3. As described, the two limiting concentrations,  $1.61$  and  $4.80\text{ M}$ , divide the concentration range into three sections, namely moderate, high and ultra-high concentrated (SiS) region, which are marked in Fig. 5b to d and previous graphs to ensure a direct comparison to the introduced model.

As already mentioned, Fig. 5b shows the coordination number  $N_c$  of oxygens in the proximity of  $\text{Li}^+$  calculated from the radial distribution function (RDF) obtained from the MD simulations. Next to the total coordination number, also the coordination numbers of the oxygens of the different ligands  $N_{c,i}$  are shown. They directly translate to the introduced model and are in very good agreement: both introduced conditions, namely  $N_c = 6$  and the coordination preference of  $\text{DME} > \text{TFSI}^- > \text{DOL}$ , are reflected. Fig. 5b shows an average coordination of  $\text{Li}^+$  by six  $\text{O}_{\text{DME}}$  in the moderate concentrated region and for ultra-high





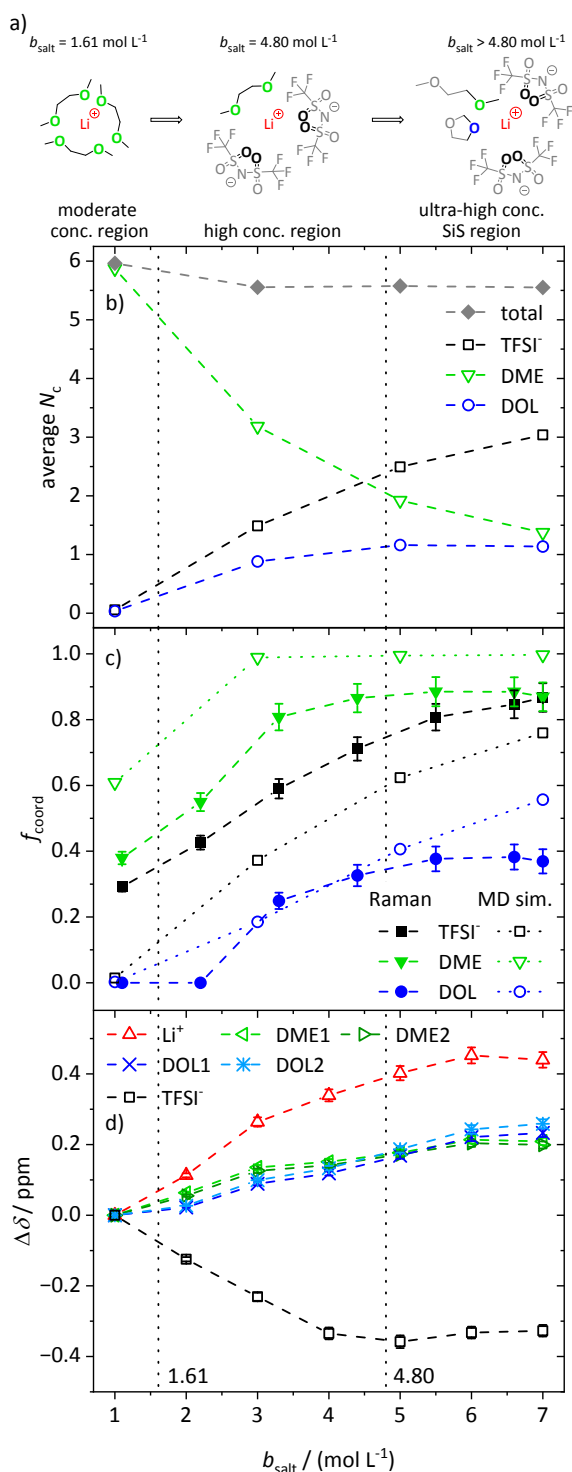


**Fig. 5** a) Illustration of the average lithium coordination shell for the introduced model based on two discussed conditions. b) Average lithium coordination number  $N_c$  of anion and solvent oxygens (open symbols) as well as the total coordination number (gray diamonds) from MD simulations. c) Fraction of coordinating molecules  $f_{\text{coord}}$  for the different species (TFSI<sup>-</sup> black squares, DME green triangles, DOL blue circles) from the Raman bands (filled symbols) as well as from MD simulations (open symbols) as a function of the conducting salt concentration. d) Chemical shift difference  $\Delta\delta$  referred to the chemical shift of the 1 M electrolyte for each investigated NMR signal. Solvent signals as explained in Scheme 1. The dashed lines in all graphs serve as guide to the eye, and the vertical dotted lines result from the model-based interpretation seen in a) marking different regimes of the lithium coordination shell.

conducting salt concentrations of 7 M in the SiS region, DME and DOL coordinate on average with one oxygen atom each and TFSI<sup>-</sup> with more than three oxygens, just as the model in Fig. 5a predicts.

However, in contrast to the model in Fig. 5a, DOL starts to coordinate lithium already at concentrations below the second limiting concentration of 4.80 M. In addition, Fig. 5b reveals a slightly reduced total  $N_c$  from 6 to 5.8 with increasing conducting salt concentration. There might be sterical hindrances in the high concentration electrolytes, which prevent a local packing with an optimized Li<sup>+</sup> coordination. In addition, entropic contributions, overcoming small energy differences of Li-oxygen interactions, may significantly broaden transitions between the regimes. Nevertheless, in spite of the simplistic nature of the model, especially concerning the high concentrated region, it is still providing a suitable guideline for the changes in the average lithium coordination shell with increasing conducting salt concentration.

Using the just discussed  $N_{c,i}$  values, we calculated the coordinating fractions of the different coordination sites  $f_{\text{coord,MD}}$  from the MD simulations results using eq. 10. Here,  $n_{\text{Li}}$  describes the total number of lithium cations and  $O_{\text{tot},i}$  the total number of oxygens of the particular species in the simulation box of a certain electrolyte formulation.

$$f_{\text{coord, MD}} = \frac{N_{c,i} \cdot n_{\text{Li}}}{O_{\text{tot},i}} \quad (10)$$

The obtained values are shown in Fig. 5c and compared to  $f_{\text{coord,Raman}}$ , calculated according to eq. 2 and based on the Raman spectra shown in the previous section.

The experimental results support the introduced model. Of the three Li<sup>+</sup>-coordinating molecules, it is DME, of which the highest fraction is coordinated, followed by TFSI<sup>-</sup> and then DOL. At high conducting salt concentration, it is again DME, reaching a plateau, where all DME molecules are coordinating, again followed by TFSI<sup>-</sup> and finally DOL, which both only reach lower maximum fractions of coordination. The transitions from a homogeneous DME-coordination (see moderate concentrated region, Fig. 5a to a mixed DME-TFSI<sup>-</sup>-coordination in the high concentrated region, and further to a mixed coordination involving DOL in the ultra-high concentrated SiS region, are not very sharp transitions. TFSI<sup>-</sup> starts to coordinate already in the moderate concentrated section and DOL starts to coordinate Li<sup>+</sup> before the second limiting concentration is reached, as already discussed.

Moreover, Fig. 5c also shows a qualitatively very good agreement between two of the used methods, namely Raman measurements and MD simulations, proving that the MD simulations are a reliable addition to experimental studies. The deviations between these two techniques can be traced to their respective uncertainties. While the deconvolution of the Raman bands may contain slight systematic deviations, the force fields used for the MD simulations describe polarization effects due to the ions only approximately, leading to deviations from the real system especially at ultra-high conducting salt concentrations where polarization effects play an important role. The same applies for the comparison of the self-diffusion



coefficients calculated from the MD simulations and measured by PFG-NMR shown in Fig. S6. Despite deviations of the absolute values in the SiS region, the MD simulations reproduce the experimentally observed trend quite well, which, in combination with the structural quantities in Fig. 5, demonstrate that the utilized force field adequately captures the most important trends of the conducting salt concentration dependence.

Finally, the coordination behavior of the different species can be analyzed experimentally by evaluating the chemical shift in dependence on the conducting salt concentration, shown in Fig. 5d. Since the chemical shift is depending on the electronic environment of a nucleus, changes in this shift,  $\Delta\delta$ , reflect changes in the coordination environment. Here, we refer the changes  $\Delta\delta$  to the shift in a molal concentration of 1 M. It has to be noted that lithium and hydrogen nuclei are dominated by diamagnetic shielding, while fluorine is mostly influenced by paramagnetic shielding, leading to an opposite shift direction.<sup>56</sup> Further, it has to be considered that chemical shifts of different nuclei, namely  $^1\text{H}$ ,  $^{19}\text{F}$ , and  $^7\text{Li}$ , are compared. Therefore, the magnitude of the change in  $\delta$  can only be compared for the two solvent molecules, since both are measured via  $^1\text{H}$  NMR spectroscopy. Exemplary stack plots of the NMR spectra for all species are shown in Fig. S7.

The changes in the chemical shift  $\Delta\delta$  shown in Fig. 5d also match the proposed model. Generally, we observed that the addition of conducting salt causes a deshielding for all investigated species due to ionic clustering. However, there are distinct differences for the different coordinating species: At lower salt concentrations, the chemical shift of DME is more strongly affected by an increasing salt concentration compared to the chemical shift of DOL. Therefore, the condition that DME coordinates  $\text{Li}^+$  rather than DOL is confirmed. The most drastic changes of the chemical shifts should occur in the high concentrated section, since, according to the model,  $\text{TFSI}^-$  starts to participate in the coordination of  $\text{Li}^+$ , which has a major impact on the local electronic environment of  $\text{Li}^+$  and all coordinating species. This is indeed apparent in the highest slope of  $\Delta\delta$  observed for  $\text{Li}^+$ ,  $\text{TFSI}^-$  and DME in this region. However, also  $\Delta\delta_{\text{DOL}}$  changes before the second limiting concentration is reached, in agreement with the MD simulations. Therefore, the evaluation of the chemical shift reproduces this slight deviation from the proposed model as discussed for Fig. 5b and c. Nevertheless,  $\Delta\delta_{\text{DOL}}$  keeps changing above the second limiting salt concentration 4.80 M, while  $\Delta\delta$

of the other species reach plateau values, which is again in agreement with the proposed model. The local electronic environment of these species and thus their chemical shift does not change significantly if one coordinating oxygen of DME is on average exchanged by an oxygen of DOL as shown in Fig. 5a.

We note, however, that Fig. 5a displays an average coordination environment. A monomodal coordination of only one oxygen of DME to  $\text{Li}^+$  seems unlikely and leads to the expectation that the coordination of DME to  $\text{Li}^+$  is occurring with both oxygens. This is supported by the distribution of *molecular* coordination numbers,  $N_{m,i}$ , shown in Fig. S8, where the average number of coordinating DME molecules,  $N_{m,\text{DME}}$ , is approximately half as large as the respective oxygen coordination numbers,  $N_{c,\text{DME}}$ , in Fig. 5b. Fig. S8 also demonstrates a certain heterogeneity of the coordination environment, as the actual *molecular* coordination numbers partly differ from the average. This increasing heterogeneity with increasing conducting salt concentration is also shown in snapshots of the MD simulation boxes, see Fig. S9.

In order to support the assumption of this heterogeneity and its consequences for transport properties, we evaluated the MD simulations in more detail, as presented in the next section.

#### Heterogeneity in $\text{Li}^+$ coordination and its impact on ion transport.

In order to obtain insights into the actual 1<sup>st</sup> coordination shell of lithium and the deviation from the proposed average model, we evaluated the distribution of coordination numbers of the oxygen atoms of the different ligands,  $\text{O}_{\text{DME}}$ ,  $\text{O}_{\text{DOL}}$ , and  $\text{O}_{\text{TFSI}}$  over the concentration range. The results are shown in Fig. 6a-d for four conducting salt concentrations. For the anions, the histograms resemble a normal distribution. Moreover, the histograms show that from a 3 M salt concentration upwards, about 40% of the lithium cations are no longer coordinated by six oxygens, but by five.

Interestingly, for DME, in contrast to DOL and  $\text{TFSI}^-$ , only even coordination numbers are found. Due to its molecular structure DME is a bidentate ligand and forms energetically favored chelate complexes with the lithium cation leading to the observed even coordination numbers. Even though  $\text{TFSI}^-$  is a bidentate ligand too, also monodentate coordination is observed in Fig. 6 for this ligand. Apparently, sterical hindrance can reduce the energy gain of a bidentate coordination. Additionally, the histograms in Fig. 6 exhibit, as expected, that



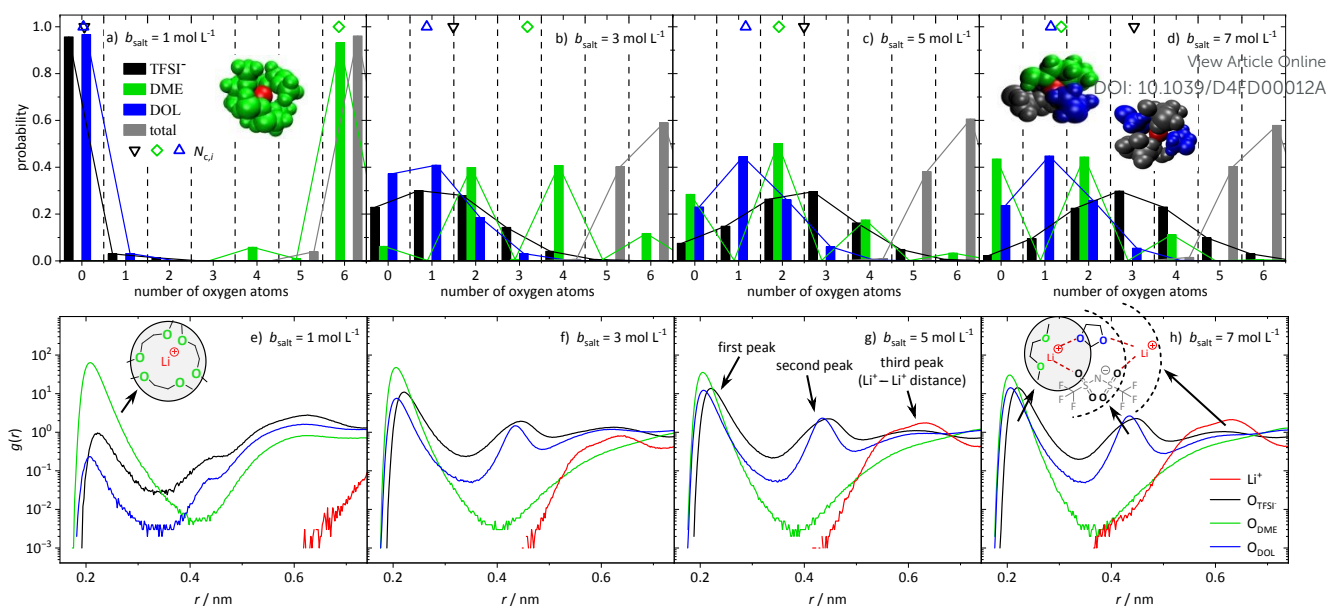


**Fig. 6** Probability of the number of oxygen atoms in the first coordination shell of  $\text{Li}^+$  and  $N_{c,j}$  (average oxygen coordination number indicated by the colored symbols at the top of each graph) for anion (black), DME (green), DOL (blue), and total (gray), for the conducting salt concentrations: a) 1 M, b) 3 M, c) 5 M, d) 7 M. The included snapshots from the MD simulations show the most frequent coordination shell of  $\text{Li}^+$  for the respective salt concentration. Lithium cations in red and the other molecules according to the colors in the histograms. Radial distribution functions  $g(r)$  in dependence of the distance  $r$  to a lithium cation for the oxygen atoms of TFSI<sup>-</sup> (black), DME (green), and DOL (blue) as well as  $\text{Li}^+$  cations (red) for the conducting salt concentrations: e) 1 M, f) 3 M, g) 5 M, h) 7 M.

the coordination structure of  $\text{Li}^+$  in the (ultra-)high concentration electrolytes is rather heterogeneous and not separated into cations still coordinated only by DME molecules and cations coordinated by anions and DOL. Similar results are obtained by analyzing the *molecular* coordinating number for the different species,  $N_{m,j}$ , shown in Fig. S6.

Since the structural properties in Fig. 5 show a good agreement between MD simulations and experiments, the radial distribution function (RDF) can be used to gain information of the global electrolyte structure in addition to the already discussed first coordination shell of the cations. Fig. 6e-h show the RDFs in dependency on the distance  $r$  to a lithium cation for the oxygen atoms of the anion and solvent molecules as well as the distance to other  $\text{Li}^+$  cations. The first peak around 0.22 nm refers to the first coordination shell of  $\text{Li}^+$ , which is already discussed above. However, the RDFs for the (ultra-)high concentrated electrolytes exhibit second peaks around 0.44 nm, which are growing with increasing amount of conducting salt. Interestingly, a second peak is only observed for DOL and the anion and not for DME. This confirms that DME coordinates as a bidentate ligand, such that both oxygens are part of the first peak in the RDF. In contrast, DOL can only coordinate monodentate due to its ring structure and similarly, the bulky TFSI<sup>-</sup> anion cannot bind with all four oxygen to the same  $\text{Li}^+$ . Thus, these oxygens occur at a larger distance from the  $\text{Li}^+$  cation and form the second peak at 0.44 nm, which is rising with increasing conducting salt concentration due to the increasing amount of TFSI<sup>-</sup> and DOL coordinating  $\text{Li}^+$ .

Analyzing the probability of certain  $\text{Li}^+ - \text{Li}^+$  distances (red line in Fig. 6e-h) it can be noticed that a peak arises at 0.6 nm, which grows with an increasing amount of conducting salt. This

illustrates for the ultra-high concentrated system, in which the oxygen-to-Li ratio is decreasing, that the TFSI<sup>-</sup> and DOL molecules in the first coordination shell of a lithium cation directly coordinate a second  $\text{Li}^+$  with their free oxygen atoms. Thus, these molecules bridge between different cations, leading to aggregation. However, this bridging behavior is impossible for DME when coordinating in a bidentate fashion. In conclusion, two different coordination environments for lithium are possible and according to Fig. 6d most frequently observed in the SiS domain. On the one hand a coordination including one DME molecule (i.e. two  $\text{O}_{\text{DME}}$ ) next to anions and DOL, and on the other hand a coordination only by anions and DOL without oxygens of DME. Regarding Fig. 6d the distribution between these two coordination environments in the 7 M electrolyte is 1:1, since the probability for counting either zero or two  $\text{O}_{\text{DME}}$  in the first coordination shell of lithium is 50%, respectively.

#### Impact of heterogeneous $\text{Li}^+$ coordination for $\text{Li}^+$ transport.

With this information about the  $\text{Li}^+$  coordination in mind, conclusions about the lithium transport mechanisms become feasible. Firstly, all the initially discussed dynamic properties, namely diffusion, relaxation, and migration, show changes in the concentration behavior according to the limiting concentrations/concentration regions based on the introduced model for the average 1<sup>st</sup> lithium coordination shell, leading to the assumption that this coordination behavior is also influencing the lithium transport mechanism. Especially, the experimental results showed that SiS electrolytes exhibit a high  $\text{Li}^+$  transference number (see Fig. 3), thus the cation is more mobile than the anion. Additionally, in this SiS concentration region it turned out that DME exhibits a faster migration in the



electric field than the cation (see Fig. 2). Considering the apparent exclusive bidentate coordination behavior of DME in contrast to the bridging properties of DOL and TFSI<sup>-</sup>, the experimental results are rather conclusive. A Li<sup>+</sup> ion with a coordination shell, which contains next to TFSI<sup>-</sup> and DOL also a DME molecule, is containing the whole DME molecule and thus is less affected by bridging to the next coordination shell, i.e. a second Li<sup>+</sup>. Therefore, Li<sup>+</sup> cations in DME-rich coordination environment can move more freely, dragging along the DME molecule. In contrast, Li<sup>+</sup> ions in coordination shells only consisting of DOL and TFSI<sup>-</sup>, are more subject to bridging and aggregation. This explains why the cation mobility is in general higher than the anion mobility resulting in the observed high lithium transference number. Clear evidence for the impact of the heterogeneous lithium coordination on transport is given by the fact that the mobility of the uncharged DME molecule is higher than that of Li<sup>+</sup> in the SIS region. In view of the heterogeneous coordination, this peculiar finding can now be explained. At ultra-high conducting salt concentration, DME is exclusively coordinated to the faster migrating Li<sup>+</sup> species, it thus has a high electrophoretic mobility. The signal of Li<sup>+</sup>, however, is averaged over DME-coordinated Li<sup>+</sup> with a high mobility, and Li<sup>+</sup> in a TFSI<sup>-</sup>/DOL coordination environment with a lower mobility, leading to  $\mu_{\text{Li}} < \mu_{\text{DME}}$ .

However, all the described effects only exist in the ultra-high concentrated, SIS electrolytes with  $b_{\text{salt}} > 4.8 \text{ mol L}^{-1}$ . Here, the oxygen-to-cation ratio is so small that the bridging properties of DOL and TFSI<sup>-</sup> dominate, which is observed by the growing Li<sup>+</sup> – Li<sup>+</sup> peak in Fig. 6e-h. This peak is observed at conducting salt concentrations higher than 4.8 M indicating an aggregated system with the discussed transport behavior.

## Conclusion

To conclude, a broad experimental investigation of the coordination structure in a bi-solvent electrolyte in dependency on the conducting salt concentration from a moderate to ultra-high concentrated, Solvent-in-Salt electrolyte formulations is performed and supported by MD simulations. The investigation yielded a basic model for the average first coordination shell of the lithium cation leading to limiting concentrations, where the coordination environment changes. These limits are also reflected in the experimental results. Therefore, changes in the dynamic properties of the electrolyte, for example the mobility, are explained by changes in the lithium coordination and thus, lithium transport mechanism.

More precisely, it is found that the preferred coordination number of six oxygen around Li<sup>+</sup> is almost reached over the whole concentration region and that DME coordinates Li<sup>+</sup> rather than TFSI<sup>-</sup> and TFSI<sup>-</sup> rather than DOL. In addition to that, the MD simulations revealed that the TFSI<sup>-</sup> and DOL molecules act as bridging ligands and coordinate more than one lithium cation at once in the ultra-high concentration electrolyte due to the low oxygen to Li<sup>+</sup> ratio. In contrast, DME is a bidentate and not a bridging ligand. Thus, this difference in the coordinating properties of the ligands in combination with the limited availability of DME molecules separate the lithium coordination

environment into two frequent coordination shells: A coordination shell including one DME molecule and a coordination without any DME. This explains the finding of a faster and a slower migrating Li<sup>+</sup> species. The first one is partly coordinated to DME, which also explains the unexpected high mobility of DME, and the second one is only coordinated by TFSI<sup>-</sup> and DOL and therefore part of a larger aggregate.

In summary, all these investigations show that merging the properties of two solvents of different lithium coordination strength with an ultra-high conducting salt concentration creates interesting transport phenomena. In particular, the heterogeneous coordination environment of Li<sup>+</sup> ions, as highlighted here, is responsible for the high lithium transference number, since it enhances the structural Li<sup>+</sup> transport in combination with an effective dynamic decoupling of Li<sup>+</sup> and anion transport with  $\sigma_{+}/\sigma_{\text{ion}} \approx 0$ . In conclusion, electrolytes with ultra-high conducting salt concentration do not only offer high performance concerning key performance indicators, but also a high  $t_{\text{Li}}$ , making them, in spite of their low ionic conductivity, promising candidates for next generation battery applications.

## Author Contributions

CRedit: A.H.: data curation, formal analysis, investigation, methodology, software, validation, visualization, writing—original draft. F.A.: investigation, methodology, validation, visualization, writing—original draft. D.D.: resources, software, writing—review and editing. I.C-L: writing—review and editing. M.S.: data curation, funding acquisition, project administration, resources, supervision.

## Conflicts of interest

There are no conflicts to declare.

## Acknowledgements

The authors thank Martin Lorenz for assistance with the repetition of an eNMR measurement. A.H. is supported by the Ministry of Culture and Science of the State North Rhine Westphalia in course of the International Graduate School for Battery Chemistry, Characterization, Analysis, Recycling and Application (BACCARA). The MD simulations for this work were performed on the computer cluster PALMA II of the University of Münster.

## References

1. D. Larcher and J. M. Tarascon, *Nat Chem*, 2015, **7**, 19-29.
2. Y. Yamada, J. Wang, S. Ko, E. Watanabe and A. Yamada, *Nat. Energy*, 2019, **4**, 269-280.
3. Y. Yamada and A. Yamada, *J. Electrochem. Soc.*, 2015, **162**, A2406-A2423.
4. Y. Ugata and N. Yabuuchi, *Trends Chem.*, 2023, **5**, 672-683.
5. V. A. Azov, K. S. Egorova, M. M. Seitkalieva, A. S. Kashin and V. P. Ananikov, *Chem. Soc. Rev.*, 2018, **47**, 1250-1284.



6. J. Alvarado, M. A. Schroeder, M. Zhang, O. Borodin, E. Gobrogge, M. Olguin, M. S. Ding, M. Gobet, S. Greenbaum, Y. S. Meng and K. Xu, *Mater. Today*, 2018, **21**, 341-353.
7. O. Borodin, L. Suo, M. Gobet, X. Ren, F. Wang, A. Faraone, J. Peng, M. Olguin, M. Schroeder, M. S. Ding, E. Gobrogge, A. von Wald Cresce, S. Munoz, J. A. Dura, S. Greenbaum, C. Wang and K. Xu, *ACS Nano*, 2017, **11**, 10462-10471.
8. M. Greenwood, J. M. Wrogemann, R. Schmuch, H. Jang, M. Winter and J. Leker, *J. Power Sources Adv.*, 2022, **14**.
9. L. G. Lu, X. B. Han, J. Q. Li, J. F. Hua and M. G. Ouyang, *J. Power Sources*, 2013, **226**, 272-288.
10. A. Manthiram, *ACS Cent. Sci.*, 2017, **3**, 1063-1069.
11. M. Winter, B. Barnett and K. Xu, *Chem. Rev.*, 2018, **118**, 11433-11456.
12. Y. Ishino, K. Takahashi, W. Murata, Y. Umebayashi, S. Tsuzuki, M. Watanabe, M. Kamaya and S. Seki, *Energy Technol.*, 2019, DOI: 10.1002/ente.201900197, 1900197.
13. H.-J. Peng, J.-Q. Huang, X.-B. Cheng and Q. Zhang, *Adv. Energy Mater.*, 2017, **7**.
14. S. Zhang, K. Ueno, K. Dokko and M. Watanabe, *Adv. Energy Mater.*, 2015, **5**, 1500117.
15. M. Armand, P. Axmann, D. Bresser, M. Copley, K. Edström, C. Ekberg, D. Guyomard, B. Lestriez, P. Novák, M. Petranikova, W. Porcher, S. Trabesinger, M. Wohlfahrt-Mehrens and H. Zhang, *J. Power Sources*, 2020, **479**.
16. G. A. Giffin, *Nat. Commun.*, 2022, **13**, 5250.
17. K. Dokko, D. Watanabe, Y. Ugata, M. L. Thomas, S. Tsuzuki, W. Shinoda, K. Hashimoto, K. Ueno, Y. Umebayashi and M. Watanabe, *J. Phys. Chem. B*, 2018, **122**, 10736-10745.
18. P. Zhou, X. Zhang, Y. Xiang and K. Liu, *Nano Res.*, 2022, **16**, 8055-8071.
19. L. Suo, Y. S. Hu, H. Li, M. Armand and L. Chen, *Nat. Commun.*, 2013, **4**, 1481.
20. A. Nakanishi, K. Ueno, D. Watanabe, Y. Ugata, Y. Matsumae, J. Liu, M. L. Thomas, K. Dokko and M. Watanabe, *J. Phys. Chem. C*, 2019, **123**, 14229-14238.
21. S. Kondou, M. L. Thomas, T. Mandai, K. Ueno, K. Dokko and M. Watanabe, *Phys. Chem. Chem. Phys.*, 2019, **21**, 5097-5105.
22. J. Self, K. D. Fong and K. A. Persson, *ACS Energy Lett.*, 2019, **4**, 2843-2849.
23. L. Suo, F. Zheng, Y.-S. Hu and L. Chen, *Chin. Phys. B*, 2016, **25**.
24. M. Holz, *Chem. Soc. Rev.*, 1994, **23**, 165.
25. M. Gouverneur, J. Kopp, L. van Wüllen and M. Schönhoff, *Phys. Chem. Chem. Phys.*, 2015, **17**, 30680-30686.
26. R. L. Vold, J. S. Waugh, M. P. Klein and D. E. Phelps, *J. Chem. Phys.*, 1968, **48**, 3831-3832.
27. H. Y. Carr and E. M. Purcell, *Phys. Rev.*, 1954, **94**, 630-638.
28. S. Meiboom and D. Gill, *Rev. Sci. Instrum.*, 1958, **29**, 688-691.
29. E. L. Hahn, *Phys. Rev.*, 1950, **80**, 580-594.
30. E. Pettersson, I. Furó and P. Stilbs, *Concepts Magn. Reso. A*, 2004, **22A**, 61-68.
31. Q. H. He and Z. H. Wei, *J Magn Reson*, 2001, **150**, 126-131.
32. F. Schmidt, A. Pugliese, C. C. Santini, F. Castiglione and M. Schönhoff, *Magn. Reson. Chem.*, 2020, **58**, 271-279.
33. A. J. Bard and L. R. Faulkner, *Electrochemical Methods: Fundamentals and applications*, Wiley New York, 2001.
34. P. Nürnberg, E. I. Lozinskaya, A. S. Shaplov and M. Schönhoff, *J. Phys. Chem. B*, 2020, **124**, 861-870.
35. Q. Zhou, P. D. Boyle, L. Malpezzi, A. Mele, J.-H. Shin, S. Passerini and W. A. Henderson, *Chem. Mater.*, 2011, **23**, 4331-4337.
36. M. J. Abraham, T. Murtola, R. Schulz, S. Pall, J. C. Smith, B. Hess and E. Lindahl, *SoftwareX*, 2015, **1-2**, 19-25.
37. W. L. Jorgensen, D. S. Maxwell and J. Tirado-Rives, *J. Am. Chem. Soc.*, 1996, **118**, 11225-11236.
38. J. N. Canongia Lopes and A. A. H. Pádua, *J. Phys. Chem. B*, 2004, **108**, 16893-16898.
39. J. N. Canongia Lopes and A. A. H. Pádua, *Theor. Chem. Acc.*, 2012, **131**.
40. R. J. Gowers, M. Linke, J. Barnoud, T. J. E. Reddy, M. N. Melo, S. L. Seyler, D. L. Dotson, J. B. Domanski, S. and I. M. B. Kenney, O., *Proc. Python Sci. Conf.*, 2016, DOI: 10.25080/majora-629e541a-00e 98-105.
41. N. Michaud-Agrawal, E. J. Denning, T. B. Woolf and O. Beckstein, *J. Comput. Chem.*, 2011, **32**, 2319-2327.
42. L. Martinez, R. Andrade, E. G. Birgin and J. M. Martinez, *J. Comput. Chem.*, 2009, **30**, 2157-2164.
43. N. Molinari, J. P. Mailoa and B. Kozinsky, *Chem. Mater.*, 2018, **30**, 6298-6306.
44. A. Thum, A. Heuer, K. Shimizu and J. N. Canongia Lopes, *Phys. Chem. Chem. Phys.*, 2020, **22**, 525-535.
45. K. Yoshida, M. Tsuchiya, N. Tachikawa, K. Dokko and M. Watanabe, *J. Phys. Chem. C*, 2011, **115**, 18384-18394.
46. R. Raccichini, J. W. Diben, A. Brew, J. R. Owen and N. García-Arárez, *J. Phys. Chem. B*, 2017, **122**, 267-274.
47. N. M. Vargas-Barbosa and B. Roling, *ChemElectroChem*, 2019, **7**, 367-385.
48. F. Schmidt and M. Schönhoff, *J. Phys. Chem. B*, 2020, **124**, 1245-1252.
49. S. Pfeifer, F. Ackermann, F. Sälzer, M. Schönhoff and B. Roling, *Phys. Chem. Chem. Phys.*, 2021, **23**, 628-640.
50. Y. Yamada, M. Yaegashi, T. Abe and A. Yamada, *Chem. Commun.*, 2013, **49**, 11194-11196.
51. P. Zeng, Y. Han, X. Duan, G. Jia, L. Huang and Y. Chen, *Mater. Res. Bull.*, 2017, **95**, 61-70.
52. K. Qian, S. Seifert, R. E. Winans and T. Li, *Energy Fuels*, 2021, **35**, 19849-19855.
53. M. Bochenska, V. C. Kravtsov and V. E. Zavadnik, *J. Inclusion Phenom. Mol.*, 1997, **28**, 125-140.
54. H. Yoshida and H. Matsuura, *J. Phys. Chem. A*, 1998, **102**, 2691-2699.
55. X. Bogle, R. Vazquez, S. Greenbaum, A. Cresce and K. Xu, *J. Phys. Chem. Lett.*, 2013, **4**, 1664-1668.
56. W. A. Henderson, N. R. Brooks, W. W. Brennessel and V. G. Young, *Chem. Mater.*, 2003, **15**, 4679-4684.



View Article Online  
DOI: 10.1039/D4FD00012A

Open Access Article. Published on 05 March 2024. Downloaded on 5/18/2024 8:49:27 AM.  
This article is licensed under a Creative Commons Attribution 3.0 Unported Licence.



Faraday Discussions Accepted Manuscript